# RSC Advances

**A study of the electronic structure and structural stability of $Gd_2Ti_2O_7$ based glass-ceramic composites**

Esther Rani Aluri and Andrew P. Grosvenor*

*Department of Chemistry, University of Saskatchewan, Saskatoon, SK, Canada, S7N 5C9*

* Author to whom correspondence should be addressed
E-mail: andrew.grosvenor@usask.ca
Phone: (306) 966-4660
Fax: (306) 966-4730

**Abstract**

Glass-ceramic composite materials have been investigated for nuclear waste sequestration applications due to their ability to incorporate large amounts of radioactive waste elements. Borosilicate- and Fe-Al-borosilicate glass-ceramic composites containing pyrochlore-type $Gd_2Ti_2O_7$ crystallites were synthesized at different annealing temperatures and investigated by multiple techniques. Backscattered electron (BSE) images were collected to investigate the interaction of the pyrochlore crystallites with the glass matrix. Examination of the X-ray absorption near edge spectroscopy (XANES) spectra from the composite materials has shown how the glass composition, pyrochlore loading, and annealing temperature affects the chemical environment around the metal centers. These investigations have shown that the $Gd_2Ti_2O_7$ crystallites can dissolve in the glass matrix depending on the glass composition and annealing temperature. The borosilicate glass composite materials were implanted with high-energy $Au^-$ ions to mimic radiation induced structural damage. Surface sensitive glancing angle XANES spectra collected from the implanted composite materials have shown that structural damage of $Gd_2Ti_2O_7$ occurs as a result of implantation, and that these materials show a similar response to ion implantation as $Gd_2Ti_2O_7$ alone.

*Keywords*: Glass-ceramic composites; Pyrochlore; Electron microscopy; XANES; Ion implantation; Nuclear waste sequestartion

## 1. Introduction:

The safe and effective disposal of nuclear waste, especially high level nuclear waste (HLW), has become a crucial issue in our increasingly industrialized and globalized society.[1-5] Extensive studies have been performed in the field of nuclear waste immobilization, leading to the development of various nuclear wasteforms that are composed of: amorphous glasses, crystalline materials, glass-ceramic composites, and casks.[4-8] A nuclear wasteform must exhibit long-term chemical durability to isolate radioactive nuclear waste from the biosphere for a sufficiently long time (i.e., thousands of years).[9-11]

Glass-ceramic composites have received attention for the immobilization (i.e., sequestration) of nuclear waste beacause of the flexible structure of these materials, which can enhance the incorporation of radioactive waste elements.[6,8,12-14] For glass-ceramic materials to be a potential nuclear wasteform, they must have a homogeneous distribution of crystalline materials in the bulk of a glass matrix, and the ability to incorporate actinides and other fission products in either the crystalline structure or the glass matrix.[13,15,16,17] The glass in these composites can also act as a secondary barrier for the radioactive waste incorporated in the crystalline material.[16-18] Glass-ceramic composite materials can exhibit varying degrees of resistance to radiation induced structural damage depending on the composition of the glass and/or the crystalline material.[4,18,19] During the decay of a radioactive element, α- and β-particles or γ-rays can be released with the radioactive element transforming to a daughter nucleide. The product of radioactive decay and its recoil energy can cause defects in the structure, as well as swelling and cracking of the materials.[9] This can affect the long-term chemical durability of the nuclear wasteform.[4,5,9] Therefore, it is important to understand how the chemistry of these materials affect their resistance to radiation induced structural damage, which

can be simulated using high energy ion beam implantation using ions such as $Au^-$, $Kr^+$, or $Xe^+$.[4,9,14,19-22]

Borosilicate glass compositions have been proposed in the past for the immobilization of nuclear waste because of the stability and flexibility of the silicate network, which can also incorporate large amounts of radioactive waste elements.[4,9,11,13,14] It has been recently demonstrated that the presence of transition metals (e.g., Fe) in the borosilicate glass can lead to an increased resistance to structural defects caused by β-particles or γ-rays.[23-26] The release of β-particles and γ-rays from radioactive elements can lead to the formation of electron-hole pairs, which can result in a change in the silicate and borate bonding networks.[23,25] Previous reports have suggested that Fe present in the glass matrix can trap the electron-hole pairs because of the redox characteristics of this element.[23,25]

Rare-earth titanate pyrochlore-type crystalline oxides have been considered as potential nuclear wasteforms because the crystal structure of these materials can incorporate actinides, with natural samples having been found to contain up to 30 wt% $UO_2$.[27-30] Pyrochlore-type oxides can be represented by the general formula $A_2B_2O_7$ (Space group: $Fd\bar{3}m$), where $A^{3+}$ and $B^{4+}$-site cations are in eight and six coordinate sites, respectively (see Figure 1).[30-32] The potential for developing glass-ceramic composites containing pyrochlore-type oxides, and the possibility of these materials to be resistant to radiation induced structural damage, has led to an increased interest in using these materials for the sequestration of nuclear waste.[12-17]

X-ray absorption near-edge spectroscopy (XANES) is a technique that can be used to investigate the changes in the electronic structure of the composite materials.[34,35] The local coordination number (CN), oxidation state, and bonding environment of the element of interest

can be determined through the analysis of the intensity, absorption energy, and line shape of the spectra.[36-39] Ion implantation can simulate radiation induced damage; however, these high-enegy ions can only implant in the near-surface region of the pellets. To selectively probe the damaged surface layer, surface sensitive glancing angle XANES (GA-XANES) can be used. During a GA-XANES experiment, which could also be refered to as grazing incidence XANES, the incident X-ray beam angle is set to be just above the critical angle (the angle at which total external reflection occurs) to selectively probe the damaged surface layer of a material.[21,40,41]

The objective of this study was to understand the interaction of pyrochlore crystallites within a glass matrix, and to investigate how these materials change as a result of ion implantation. Composite materials consisting of a borosilicate (and Fe-Al-borosilicate) glass matrix containing $Gd_2Ti_2O_7$ pyrochlore-type crystallites have been synthesized using different annealing temperatures. Electron microscopy and powder X-ray diffraction (XRD) have been used to study how the $Gd_2Ti_2O_7$ crystallites dispersed in the glass matrix. The interaction of $Gd_2Ti_2O_7$ in the glass matrix has been examined before and after ion implantation by collecting Ti K-edge (GA-)XANES spectra. Si $L_3$-, Fe K-, and Al $L_3$-edge XANES spectra were also collected to investigate how the electronic structure of the glass changes depending on $Gd_2Ti_2O_7$ loading, the glass composition, and the annealing temperature used to make these composite materials.

## 2. Experimental

### 2.1. Synthesis

Borosilicate glass (BG), Fe-Al-borosilicate glass (FABG), and glass-pyrochlore composites (BG/FABG-$Gd_2Ti_2O_7$) were synthesized by a conventional solid state method. The

compositions of the borosilicate and Fe-Al-borosilicate glasses are listed in Table 1. Appropriate amounts of the respective metal oxide powders were mixed using a mortar and pestle and placed in graphite crucibles. The mixtures were annealed at 1100 $^{\circ}$C for 1 hour in air to produce the glass materials. The amorphous structure was confirmed by examination of powder XRD data. Diffraction patterns from each sample were collected at room temperature using a PANalytical Empyrean X-ray diffractometer and a Co K$\alpha_{1,2}$ X-ray source. The phase analysis was determined using the High Score Plus software package.[42] The synthesized borosilicate glass and Fe-Al-borosilicate glass powders were re-annealed in air at 750 $^{\circ}$C for 1 hour and the phases of these samples were analysed using powder XRD. Fe-borosilicate glass (FBG) and Al-borosilicate glass (ABG) samples were also synthesized to aid in analysis of the XRD patterns. The compositions of these glasses are also listed in Table. 1.

Gd$_2$Ti$_2$O$_7$ was synthesized using the ceramic method. Gd$_2$O$_3$ (Alfa Aesar, 99.99%) and TiO$_2$ (Alfa Aesar, 99.9%) powders were mixed in stoichiometric amounts using a mortar and pestle and pressed into pellets uniaxially at 6 MPa. The pellets were heated in air at 1400 $^{\circ}$C for 6 days with intermediate mixing and pelleting. The phase purity of Gd$_2$Ti$_2$O$_7$ was confirmed by powder XRD.

Different weight percentages of Gd$_2$Ti$_2$O$_7$ (10 wt% to 90 wt%) were mixed with the borosilicate glass (BG) to form the glass-pyrochlore composites. Gd$_2$Ti$_2$O$_7$ and BG were ground using a mortar and pestle to produce particles of $\leq$ 100 $\mu$m in size, pressed into pellets uniaxially at 6 MPa, and then placed in graphite crucibles. The pellets were heated in air at 1100 $^{\circ}$C or 750 $^{\circ}$C for 1 hour. All composite materials were quench cooled in air and were observed to be glass beads after annealing. Similarly, FABG-pyrochlore composites (10 wt% to 90 wt% loadings of Gd$_2$Ti$_2$O$_7$) were also formed at different annealing temperatures (1100 $^{\circ}$C and 750

$^o$C). The phase analysis of these composite materials was performed using powder XRD. The labels used to name the glasses and glass-ceramic composites studied are listed in Table 2.

## 2.2. Electron microprobe analysis

Backscattered electron images (BSE) and energy dispersive X-ray spectroscopy (EDX) spectra were collected using a JEOL 8600 electron microprobe instrument. The glass-pyrochlore composite beads were mounted in a polymer resin and the surface of the beads was polished to a smooth surface using diamond paste. The samples were coated with a conductive carbon coating prior to introducing them into the instrument. BSE images were collected from the borosilicate glass composite materials (20 wt% and 40 wt% loading of $Gd_2Ti_2O_7$ annealed at 1100 $^o$C; 20 wt%, 40 wt%, and 60 wt % loading of $Gd_2Ti_2O_7$ annealed at 750 $^o$C) at 1000X magnification. BSE images were also collected from the composite materials before and after ion implantation using a magnification of 100X. EDX spectra were collected to determine the chemical composition at different locations in each sample.

## 2.3. Ion beam implantation

The borosilicate glass-pyrochlore composites (40 wt% loading of $Gd_2Ti_2O_7$ annealed at 1100 $^o$C; 20 wt%, 40 wt%, and 60 wt% loading of $Gd_2Ti_2O_7$ annealed at 750 $^o$C) were implanted with high energy (2 MeV) Au$^-$ ions using the 1.7 MV Tandetron accelerator located at Interface Science Western (ISW), University of Western Ontario. The polished side of each glass-ceramic composite bead (see section 2.2) was implanted to a dose of $5 \times 10^{14}$ ions/cm$^2$. The ion beam was aligned normal to the glass-ceramic bead surface during implantation. As was stated in earlier reports, the 2 MeV Au$^-$ ions were calculated to implant to a maximum depth of ~450 nm in $Gd_2Ti_2O_7$.[40,41] The ion implantation depth profile calculated previously for $Gd_2Ti_2O_7$ was used in

this study based on the the assumption that pyrochlore crystallites are located at the surface of the polished glass-ceramic composite beads that were exposed to the Au$^-$ ion beam.

## 2.4. XANES

Ti K- and Fe K-edge XANES spectra were collected from as-synthesized BG-Gd$_2$Ti$_2$O$_7$ and FABG-Gd$_2$Ti$_2$O$_7$ (20 wt%, 50 wt%, and 80 wt% of Gd$_2$Ti$_2$O$_7$) composite materials annealed at 1100 $^o$C and 750 $^o$C. The spectra were collected using the Canadian Light Source/X-ray Science Division Collaborative Access Team (CLS/XSD, Sector 20) bending magnetic beamline (20BM) located at the Advanced Photon Source (APS), Argonne National Laboratory.[43] A Si (111) double crystal monochromator with harmonic rejection was used, which provides a photon flux of $\sim 10^{11}$ photons/s. The spectral resolution is 0.7 eV at 4966 eV (Ti K-edge) and 1.0 eV at 7112 eV (Fe K-edge).[43] Samples were prepared by sealing finely ground powder between layers of Kapton tape, and the thickness was varied by adding or removing layers of powder between tape to maximize the absorption-edge step height. The spectra were recorded in transmission mode using ionization chambers filled with He$_{(g)}$ and N$_{2(g)}$ (80% He:20% N$_2$ for the Ti K-edge and 0% He:100% N$_2$ for the Fe K-edge) to achieve optimal absorption-edge step heights and signal-to-noise ratios. XANES spectra were collected using a step size of 0.15 eV through the Ti K- and Fe K-edges. The Ti K-edge spectra were calibrated using Ti metal (4966 eV), and the Fe-edge spectra were calibrated using Fe metal (7112 eV).[44]

Ti K-edge GA-XANES analysis of the ion implanted pellets of the glass-ceramic composites was also performed (using the 20 BM beamline located at the APS) by vertically focusing the X-ray beam to yield a beam height of 0.15 mm while maintaining the beam width at 1 mm. Ti K-edge GA-XANES spectra were collected in fluorescence mode using a single element vortex silicon drift detector and a step size of 0.25 eV through the absorption edge. A

motor driven Huber (goniometer) stage was used to change the X-ray beam angle of incidence. The goniometer stage permits x-, y-, and z-axis translation as well as rotation of the angle ($\alpha$) between the X-ray beam and the surface of the sample. The angle ($\alpha$) was set to the desired glancing angle with an accuracy of $0.1^{\circ}$ to reach different depths of the sample. A web based program was used to calculate the glancing angles required to reach specific X-ray attenuation depths for photons having energies of 4966 eV (Ti K-edge; see Table 3).[45]

The Si $L_{2,3}$-edge and Al $L_{2,3}$-edge XANES spectra from the undamaged BG-$Gd_2Ti_2O_7$ and FABG-$Gd_2Ti_2O_7$ composite materials were measured using the Variable Line Spacing-Plane Grating Monochromator (VLS-PGM; 11ID-2) beamline at the Canadian Light Source (CLS).[46] The samples were prepared by placing finely ground powder on carbon tape. The spectra were collected in total fluorescence yield mode (TFY) using a step size of 0.05 eV through the Si absorption edge and 0.025 eV through the Al absorption edge. The spectra were calibrated using elemental Si for the Si $L_{2,3}$-edge (99.40 eV) and Al metal for the Al $L_{2,3}$-edge (72.55 eV).[44] Analysis of all XANES spectra was performed using the Athena software program.[47]

## 3. Results and discussion

### 3.1. Powder X-ray diffraction

Powder XRD patterns from the glasses and glass-pyrochlore composite materials were collected to gain information about the different phases that are present in these materials. The XRD patterns from the composite materials annealed at 1100 $^{\circ}$C and 750 $^{\circ}$C are shown in Figures 2 and 3, respectively. The patterns from the glasses annealed at 1100 $^{\circ}$C (BG-1100 $^{\circ}$C and FABG-1100 $^{\circ}$C) show only a broad hump in the region of 20-30$^{\circ}$ (Figure 2), which confirms the amorphous structure of these materials. The diffraction pattern from the borosilicate glass

annealed at 750 $^{\circ}$C shows peaks representative of quartz ($SiO_2$) along with a broad amorphous hump (Figure 3a), whereas the diffraction pattern from the FABG sample annealed at 750 $^{\circ}$C shows only a broad hump (Figure 3b). This observation indicates that quartz ($SiO_2$) was formed from the amorphous silicate network when the borosilicate glass (BG) was annealed at 750 $^{\circ}$C; however, the amorphous nature of the Fe-Al-borosilicate glass (FABG) was stable when annealed at this temperature (*c.f.* Figure 3).[48] The stabilization of the amorphous structure of the FABG sample was assumed to be a result of the presence of Fe and/or Al. The XRD patterns from the Fe- or Al- only containing borosilicate glass (i.e., FBG or ABG) samples annealed at 750 $^{\circ}$C (i.e., FBG-750 $^{\circ}$C, ABG-750 $^{\circ}$C) were collected to aid in the analysis of the stabilization of FABG-750 $^{\circ}$C and these patterns are shown in Figures 3c and 3d. Diffraction peaks indicating the presence of quartz are observed in the pattern from the FBG sample but not in the pattern from the ABG sample, which indicates that $Al_2O_3$ is responsible for stabilizing the amorphous structure of the Fe-Al-borosilicate glass regardless of annealing temperature. The small addition of aluminum oxide ($Al_2O_3$), as a network modifier, can break $SiO_4^{4-}$ tetrahedral bridging bonds and stabilize the amourphous structure of the glass so as to not allow depolymerization of the glass network to occur.[14,49,50] The presence of Aluminum oxide in the FABG sample helps to stabilize the amorphous structure of this material relative to the BG sample.

Powder XRD patterns were collected from all glass-ceramic composite materials and are shown in Figures 2 and 3. Diffraction peaks from crystalline $Gd_2Ti_2O_7$ as well as a broad hump are observed in the patterns from the BG-$Gd_2Ti_2O_7$-1100 $^{\circ}$C, FABG-$Gd_2Ti_2O_7$-1100 $^{\circ}$C, and FABG-$Gd_2Ti_2O_7$-750 $^{\circ}$C composite materials (Figures 2a, 2b, and 3b). The patterns from the BG-$Gd_2Ti_2O_7$-750 $^{\circ}$C materials that contain different loadings of $Gd_2Ti_2O_7$ (Figure 3a) contain diffraction peaks from $Gd_2Ti_2O_7$ and quartz, as well as a broad hump that is representative of a

glass. The observed decrease in the intensities of the diffraction peaks from quartz with an increase in the loading of $Gd_2Ti_2O_7$ (Figure 3a) is mainly caused by the progressive increase in the difference of the average scattering power between materials that contain diffirent loadings of $Gd_2Ti_2O_7$ and quartz.

Examination of the patterns from the composite materials annealed at 1100 $^o$C (Figure 2) shows that the minimum $Gd_2Ti_2O_7$ loading where the pyrochlore phase peaks started to appear in the diffraction patterns is 40 wt%. This indicates that some of the $Gd_2Ti_2O_7$ crystallites dissolved in the glass when the composite materials were annealed at 1100 $^o$C. However, the patterns from the composite materials annealed at 750 $^o$C (Figure 3) showed the diffraction peaks from $Gd_2Ti_2O_7$ in all of the composite materials studied. These observations indicate that the low annealing temperature (i.e., 750 $^o$C) favours the formation of a composite material with a negligible amount of pyrochlore dissolving in the glass matrix.

## 3.2. Electron microscopy

Backscattered electron (BSE) images from the borosilicate glass composites annealed at 750 $^o$C or 1100 $^o$C are shown in Figure 4. BSE images are helpful for obtaining compositional maps of a sample, and for identifying phases depending on the average atomic number.[51] The BSE images from the borosilicate glass composite materials (Figure 4) show that the pyrochlore crystallites (bright area) are distributed in the glass matrix (dark area). Pores are observed in the glass matrix because of air bubble formation during annealing.

The BSE images from the composite materials annealed at different temperatures (Figures 4a-4e) shows that the grain size of the pyrochlore crystallites are observed to be smaller in the composite materials annealed at the highest temperature (1100 $^o$C). The BSE images

(Figure 4d-e) collected from the composites annealed at 1100 $^{\circ}$C shows that the $Gd_2Ti_2O_7$ crystallites completely dissolved in the glass matrix containing a low (20 wt %) loading of $Gd_2Ti_2O_7$ while some crystallites remained when a higher (40 wt%) loading of $Gd_2Ti_2O_7$ was present. Examination of EDX spectra (Figure S1a in supporting information) collected from different locations in the BG-$Gd_2Ti_2O_7$-1100 $^{\circ}$C sample containing a 40 wt% loading of $Gd_2Ti_2O_7$ shows that the regions in the micrographs (see Figure 4e) that appear glass-like contain high concentrations of Gd and Ti. The BSE images and EDX spectra (Figure 4e and S1a) confirms that $Gd_2Ti_2O_7$ crystallites dissolved in the glass matrix after annealing the mixture at 1100 $^{\circ}$C. However, only a small fraction of the $Gd_2Ti_2O_7$ crystallites dissolved in the glass matrix of the composite materials annealed at 750 $^{\circ}$C (see Figures 4a-c and S1). These observations are in agreement with the powder XRD analysis presented above. BSE images were also collected from the ion implanted composite materials and are compared to those from the as-synthesized materials in Figure S2. The morphology and grain size of the $Gd_2Ti_2O_7$ crystallites in the glass matrix were observed to be similar when comparing the as-synthesized and ion implanted materials.

### 3.3. XANES analysis of the as-synthesized materials

XANES spectra are sensitive to changes in the electronic structure and coordination environment of atoms/ions in materials.[34,35] Examination of Ti K-, Fe K-, Si $L_{2,3}$-, and Al $L_{2,3}$-edge XANES spectra from the glass-ceramic composites has allowed for a study of how the annealing temperature, glass composition, and the loading of $Gd_2Ti_2O_7$ affected the local environment of atoms of these elements.

### 3.3.1. Ti K-edge XANES

The Ti K-edge XANES spectra from the as-synthesized BG-$Gd_2Ti_2O_7$ and FABG-$Gd_2Ti_2O_7$ composite materials (20 wt%, 50 wt%, and 80 wt% loading of $Gd_2Ti_2O_7$) annealed at either 1100 $^o$C or 750 $^o$C are shown in Figures 5 and 6, respectively. The spectrum from $Gd_2Ti_2O_7$, which was reported previously, is also presented in these figures.[41] Examination of the Ti K-edge spectra has allowed for a study of how changes in the loading of $Gd_2Ti_2O_7$ in the composite materials and the annealing temperature has affected the local coordination environment of Ti. The spectra result from 1s→3d (quadrapolar; pre-edge (A)) and 1s→4p (dipolar; main-edge (B,C)) transitions.[52-55] The pre-edge region (features $A_1$, $A_2$, and $A_3$) shows peaks that result from 1s→3d $t_{2g}$ ($A_1$), 1s→3d $e_g^*$ ($A_2$), and intersite-hybrid ($A_3$) excitations when Ti is in a 6-coordinate environment (i.e., in $Gd_2Ti_2O_7$).[54-56]

All of the pre-edge and main-edge features (A,B,C) in the spectra were found to change significantly by varying the loading of $Gd_2Ti_2O_7$ in the composite materials or the annealing temperature. The intensity of the pre-edge feature (A) decreased while the energy (B) and intensity (C) of the main-edge feature increased as the loading of $Gd_2Ti_2O_7$ increased in the composite materials (Figures 5 and 6). These changes in the Ti K-edge XANES spectra have been shown in the past to be a result of an increase in the CN of $Ti^{4+}$.[38,39,56-59] The observed increase in Ti CN suggests that the amount of $Gd_2Ti_2O_7$ dissolved in the glass matrix decreases as the loading of $Gd_2Ti_2O_7$ in the composite materials, which is in agreement with the powder XRD and electron microscopy results. The spectra from the composite materials having a low wt% of $Gd_2Ti_2O_7$ show that Ti occupies a low coordinationate environment when $Gd_2Ti_2O_7$ dissolved in the glass; Ti was found to adopt a similar coordination environment in amorphous metal silicates previously investigated by this research group.[56,38]

Examination of the spectra from the borosilicate and Fe-Al-borosilicate glass composite materials containing the same $Gd_2Ti_2O_7$ loading and annealed at 1100 °C (Figure 7a) shows that less $Gd_2Ti_2O_7$ dissolved in the Fe-Al-borosilicate glass as compared to the borosilicate glass. Only a small change was observed in the spectra from the composite materials annealed at 750 °C when compared to the spectra from $Gd_2Ti_2O_7$ (Figure 7b). These observations indicate that the FABG glass composition and lower annealing temperature favours the formation of composite materials with a small amount of the pyrochlore crystallites having dissolved in the glass, which is in agreement with the XRD and electron microscopy results.

### 3.3.2. Si L$_{2,3}$-edge XANES

Si $L_{2,3}$-edge XANES spectra were also collected to study how the Si environment was affected by varying the loading of $Gd_2Ti_2O_7$, annealing temperature, and the type of glass used. Normalized Si $L_{2,3}$-edge XANES spectra from the borosilicate glasses annealed at 1100 °C or 750 °C are shown in Figure 8. The spectra are compared to a previously reported spectrum of amourphous $SiO_2$.[56] The Si $L_{2,3}$-edge spectra exhibit two features that result from 2p→3s (Feature D) and 2p→3d (Feature E) transitions, respectively.[56] The low-energy region feature (D) is split into two peaks (D$_1$ and D$_2$), which result from $2p_{3/2}$→3s (D$_1$) and $2p_{1/2}$→3s (D$_2$) because of spin-orbit splitting.[60-63]

Comparision of the spectra from the borosilicate glasses annealed at 750 °C or 1100 °C to the spectrum from amorphous $SiO_2$ (Figure 8) reveals a significant difference in the line shapes. Feature D and E become narrower to higher energy in the spectra from the borosilicate glass annealed at 750 °C or 1100 °C as compared to the spectrum from amorphous $SiO_2$. Previous studies of various metal containing amorphous silicates and quartzes have shown that these

features become narrower to higher energy as the materials change from amorphous silicates to quartzes.[64,66] These changes are attributed to an increase in the degeneracy of the Si-O states because of a more ordered $SiO_4^{4-}$ tetrahedral bond network in the quarz lattice.[63-66] This is also supported by the presence of quartz in the XRD pattern from the borosilicate glass annealed at 750 $^o$C (see Figure 3a). The width of the features in the spectra from the composite materials were observed to decrease (Figure 9 and 10) with increasing loading of $Gd_2Ti_2O_7$. The observed changes in the spectra are attributed to changes in the ordering of the glass, including crystallization of quartz, and because of variations in the glass composition as a result of the pyrochlore crystallites dissolving in the glass which may lead to next-nearest-neighbour effects between the metal cations and Si.[63-66] These observations suggest that both the loading of $Gd_2Ti_2O_7$ in the composite *and* the annealing temperature affect the silicate network in the glass-ceramic composite materials.

### 3.3.3. Fe K-edge XANES

Fe K-edge XANES spectra (Figure 11) were collected to study the redox chemistry of Fe in the Fe-Al-glass (FABG) and Fe-Al-glass-ceramic composites (FABG-$Gd_2Ti_2O_7$) when annealed at different temperatures. The spectrum from the FABG sample is compared to the previously reported spectra from FeO ($Fe^{2+}$) and $Fe_2O_3$ ($Fe^{3+}$) in Figure 11a.[67,68] The spectra contain both pre-edge (1s→3d) and main-edge (1s→4p) excitations like in the Ti K-edge XANES spectra.[39,60,69] Comparison of the absorption edge energy (Figure 11a) of the spectra from FABG, FeO, and $Fe_2O_3$ shows that both $Fe^{3+}$ and $Fe^{2+}$ exist in the glass.

The spectra from the composite materials (20 wt%, 50 wt%, and 80 wt% loading of $Gd_2Ti_2O_7$) annealed at 1100 $^o$C and 750 $^o$C are shown in Figures 11b and 11c, and are compared

to the spectrum from FABG. The intensity and energy of features A, B, or C do not change considerably in the spectra (Figure 11b and 11c) when the loading of $Gd_2Ti_2O_7$ was varied. However, the intensity and absorption energy of features A and B do change when comparing the spectra from FABG-$Gd_2Ti_2O_7$-1100 $^o$C/750 $^o$C to the spectrum from FABG. A shift of the absorption edge to lower energy was observed in the composite materials annealed at 1100 $^o$C (Figure 11b) whereas the absorption edge shifted to higher energy when the composite materials were annealed at 750 $^o$C (Figure 11c). The energy of the pre-edge peak (A) in Fe K-edge XANES spectra has been observed previously to not be affected significantly by changes in the Fe CN.[59,60,68,69] Therefore, the observed shifts in energy of both the pre-edge (A) and main-edge (B) features in the Fe K-edge XANES spectra in Figure 11 from the composite materials annealed at 750 $^o$C or 1100 $^o$C are a result of variations in the oxidation state of Fe. Comparision of the spectra from FABG-$Gd_2Ti_2O_7$-750 $^o$C and FABG shows that the oxidation state of Fe in the glass matrix is completely oxidized to 3+ when the composite system was annealed at 750 $^o$C (*cf.* Figures 11a and 11c). Further, examination of the spectra from FABG-$Gd_2Ti_2O_7$-1100 $^o$C and FABG shows that the oxidation state of Fe in the glass was reduced to 2+ when the composite materials were annealed at 1100 $^o$C (*cf* . Figures 11a and 11b). As stated earlier, the intensity of the pre-edge feature (A) in transition metal K-edge XANES spectra can change as a result of a variation of the CN of the metal.[39,68,69] The intensity of the pre-edge feature decreased in the spectra from FABG-$Gd_2Ti_2O_7$-750 $^o$C compared to the spectrum from the as-synthesized FABG sample (Figure 11c) while the pre-edge peak intensity in the spectrum from FABG-$Gd_2Ti_2O_7$-1100 $^o$C was observed to be more intense compared to the spectrum from as-synthesized FABG (Figure 11b). The changes observed here suggest that the CN of Fe decreases

when the composite materials were annealed at 750 $^{\circ}$C and that the CN of Fe increases when the composite materials were annealed at 1100 $^{\circ}$C.

The observed changes in Fe oxidation state by varying the annealing temperature are a result of a redox reaction between oxygen and Fe. The Fe K-edge XANES spectra show that Fe in the composite materials was reduced to $Fe^{2+}$ when annealed at 1100 $^{\circ}$C and oxidized to $Fe^{3+}$ when the composites were annealed at 750 $^{\circ}$C, which can be described by the following equilibrium reaction: $4Fe^{3+}+2O^{2-} \underset{>T}{\overset{<T}{\rightleftharpoons}} 4Fe^{2+}+O_2$.[70-73] The reduction of $Fe^{3+}$ to $Fe^{2+}$ at 1100 $^{\circ}$C may also be caused by $Gd_2Ti_2O_7$ crystallites dissolving in the glass matrix when the composite materials were annealed at this temperature. These observations indicate that the oxidation state and CN of Fe in the composite materials are strongly affected by the annealing temperature.

### 3.3.4. Al L$_{2,3}$-edge XANES

Al L$_{2,3}$-edge XANES spectra were collected from the FABG-composite materials annealed at different temperatures (see Figure S3 in supporting information). The spectra consist of two features D and E, which result from 2p$\rightarrow$3s and 2p$\rightarrow$3d transitions, respectively.[74] Al L$_{2,3}$-edge XANES spectra have been shown previously to be sensitive to changes in the Al CN.[74] Examination of the spectra from the FABG-Gd$_2$Ti$_2$O$_7$ composite materials (Figure S2) show negligible changes in the spectral features with changes in loading or annealing temperature. These observations indicate that the Gd$_2$Ti$_2$O$_7$ loading and annealing temperature do not significantly affect the coordination environment of Al in the composite materials.

### 3.4. Ti K-edge GA-XANES of the ion-implanted materials

Glancing angle XANES (i.e., GA-XANES) spectra were collected from ion implanted composite samples to study how the local environment of Ti in the materials change as a result of ion-beam implantation. As was reported previously, 2 MeV Au$^-$ ions penetrate to a maximum depth of ~450 nm in $Gd_2Ti_2O_7$.[40,41] Ti K-edge GA-XANES spectra were collected using glancing angles of 1.4$^o$, 4.5$^o$, and 45$^o$, which provide X-ray attenuation depths of 220 nm, 450 nm, and 4088 nm, respectively.

Normalized Ti K-edge GA-XANES spectra from BG-$Gd_2Ti_2O_7$-1100 $^o$C (60 wt% loading of $Gd_2Ti_2O_7$) and BG-$Gd_2Ti_2O_7$-750 $^o$C (20 wt%, 40 wt%, and 60 wt% loading of $Gd_2Ti_2O_7$) implanted using Au$^-$ ions to a dose of $5\times10^{14}$ ions/cm$^2$ are shown in Figure 12. The spectra from the as-synthesized composite materials are also presented. Compared to the spectrum from as-synthesized materials, the intensity of the pre-edge peak (A) increased while the intensity and energy of the main-edge peak (B,C) decreased as a result of ion implantation.[21,40,41] These changes are indicative of a decrease in Ti CN because of ion implantation. The observed decrease in Ti CN indicates that ion implantation damages the structure of $Gd_2Ti_2O_7$ in the composite materials.[40,41] GA-XANES spectra collected at different glancing angles from the ion implanted composite materials annealed at 750 $^o$C or 1100 $^o$C (Figure 12) shows that more damage occurs near the surface compared to deeper into the material. A comparision of the spectra collected at a glancing angles providing the same X-ray attenuation depth from ion-implanted BG-$Gd_2Ti_2O_7$-750 $^o$C and $Gd_2Ti_2O_7$ (Figure 13) shows that the damage experienced by $Gd_2Ti_2O_7$ in the composite materials was similar to that experienced by the sample that only contained $Gd_2Ti_2O_7$.

## 4. Conclusions

A greater understanding of glass-ceramic composites has been achieved by the examination of pyrochlore-containing glass-composite materials by XRD, electron microscopy, and XANES. Glass-ceramic composite materials were synthesized at 1100 $^{\circ}$C and 750 $^{\circ}$C; however, $Gd_2Ti_2O_7$ was observed to dissolve significantly in the glass matrix when annealed at 1100 $^{\circ}$C. Examination of Ti K-edge XANES spectra from the composite materials show that the use of a Fe-Al-borosilicate glass and a lower annealing temperature favours the formation of a composite material being formed with only a small fraction of the $Gd_2Ti_2O_7$ crystallites dissolving in the glass matrix. The Si $L_{2,3}$-edge XANES spectra showed that the ordering of the silicate network changes depending on the glass composition, loading of $Gd_2Ti_2O_7$, and annealing temperature used to form the composite materials. Further, examination of Fe K-edge XANES spectra from the Fe-Al-borosilicate composites showed that the oxidation state of Fe changed depending on the annealing temperature used to form these composite materials. Examination of Ti K-edge GA-XANES spectra from the ion implanted composite materials has shown that the damage experienced by $Gd_2Ti_2O_7$ in the composite materials *vs* the pure ceramic (i.e., $Gd_2Ti_2O_7$) is similar. The study of these composite materials will be useful for the further development of glass-ceramic composites as potential nuclear wasteforms.

## 5. Acknowledgements

**References:**

1    L. L. Hench, D. E. Clark and J. Campbell, *Nucl. Chem. Waste manage.*, 1984, **5**, 149-173.

2    W. M. Manning, *J. Am. Chem. Soc.*, 1962, **84**, 315–315.

3    G. Taubes, *Science*, 1964, **263**, 629.

4   R. C. Ewing, W. J.  Webert and F.W. Clinard, *Prog. Nucl.  Energy*, 1995, **29**, 63-121.

5   R. C. Ewing, *Can. Mineral.*, 2005, **43**, 2099-2116.

6   W. E. Lee, M. I. Ojovan, M. C. Stennett and N. C. Hyatt, *Adv. Appl. Ceram.*, 2006, **105 (1)**, 1-12.

7   W. J. Weber, A. Navrotsky, S. Stefanovsky, E. R. Vance and E. Vernaz, *MRS Bull.*, 2009, **34**, 46-53.

8   J. Amoroso, J. C. Marra, M. Tang, Y. Lin, F. Chen, D. Su and K. S. Brinkman, *J. Nucl. Mater.*, 2014, **454**, 12–21.

9   W. J. Weber, R. C. Ewing, C. R. A. Catlow, T. D. Rubia, L. W. Hobbs, C. Kinoshita, H. Matzke, A. T. Motta, M. Nastasi and E. K. H. Salje, *J. Mater. Res*., 1998, **13 (6)**, 1434-1484.

10  I. W. Donald, B. L. Metcalfe and N. J. Taylor, *J. Mater. Sci.*, 1997, **32**, 5851-5887.

11  M. I. Ojovan and W. E. Lee, Elsevier, Amsterdam, 2005.

12  P. Loiseau and D. Caurant, *J. Nucl. Mater.*, 2010, **402**, 38–54.

13  A. R. Boccaccini, E. Bernardo, L. Blain and D. N. Boccaccini, *J. Nucl. Mater.,* 2004*, ***327**, 148–158.

14  D. Caurant, P. Loiseau, I. Bardez and C. Gervais, *J. Mater. Sci.*, 2007, **42**, 8558–8570.

15  S. Pace, V. Cannillo, J. Wu, D. N. Boccaccini, S. Seglem and A. R. Boccaccini, *J. Nucl. Mater.,* 2005, **341**, 12–18.

16  Y. Zhang, Z. Zhang, G. Thorogood and E. R. Vance, *J. Nucl. Mater.*, 2013, **432**, 545-547.

17  A. A. Digeos, J. A. Valdez, K. E. Sickafus, S. Atiq, R. W. Grimes and A. R. Boccaccini, *J. Mater. Sci.*, 2003, **38**, 1597-1604

18  A. R. Boccaccini, S. Afiq and R. W. Grimes, *Adv. Eng. Mater.*, 2003, **5**, 501-508.

19  C. J. M. Northrup, G. W. Arnold and T. J. Headley, *MRS Proc.*, 1980, **6**, 667.

20  G. Sattonnay, S. Moll, L. Thomé, C. Decorse, C. Legros, P. Simon, J. Jagielski, I. Jozwik and I. Monnet, *J. Appl. Phys.*, 2010, **108**, 103512.

21  D. P. Reid and N. C. Hyatt, *Nucl. Instru. Met. Phys. Res. B*, 2010, **268,** 1847-1852.

22  J. Lian, K. B.  Helean, B. J. Kennedy, L. M. Wang, A. Navrotsky and R. C. Ewing, *J. Phys. Chem. B*, 2006, **110**, 2343-2350.

23  O. J. McGann, P. A. Bingham, R. J. Hand, A. S. Gandy, M. Kavcic, M. Z. itnik, K. Bucar, R. Edge and N. C. Hyatt, *J. Nucl. Mater.*, 2012, **429**, 353–367.

24  E. Malchukova, B. Boizot, G. Petite and D. Ghaleb, *Eur. Phys. J. Appl. Phys.*, **45**, 10701.

25  O. J. McGann, A. S. Gandy, P. A. Bingham, R. J. Hand and  N. C. Hyatt, *MRS Proc.*, 2013, **1518**, 41-46.

26  V. Magnien, D. R. Neuville, L. Cormier, J. Roux, J. L. Hazemann, O. Pinet and P. Richet, *J. Nucl. Mater.*, 2006, **352**, 190–195.

27  J. Lian, J. Chen, L. M. Wang and R. C. Ewing, *Phys. Rev. B*, 2003, **68**, 134107.

28  J. Chen, J. Lian, L. M. Wang and R. C. Ewing, *Appl. Phys. Lett.*, 2001, **79**, 1989-1992.

29  K. B. Helean, S. V. Ushakov, C. E. Brown, A. Navrotsky J. Lian, R. C. Ewing, J. M. Farmer and L. A. Boatner, *J. Solid State Chem.*, 2004, **177**, 1858–1866.

30  R. C. Ewing, W. J.  Weber and J.  Lian, *J. Appl. Phys.*, 2004, **95**, 5949-5971.

31  M. A. Subramanian, G. Aravamudan and G. V. S. Rao, *Prog. Solid State Chem.*, 1983, **15**, 55-143.

32  B. C. Chakoumakos, *J. Solid State Chem.,* 1984, **53**, 120-129.

33  K. Momma and F. Izumi, *J. Appl. Crystallogr.* **2008**, 41, 653–658.

34  F. M. F. de Groot, *Chem. Rev.*, 2001, **101**, 1779-1808.

35  F. M. F. de Groot, *J. Elect. Spectr. Relat. Phenom.*, 1994, **67**, 529-622.

36  G. A. Waychunas, *Am. Mineral.*, 1987, **72**, 89–101.

37  E. R. Aluri and A. P. Grosvenor, *Phys. Chem. Chem. Phys.*, 2013, **15**, 10477-10486.

38  M. W. Gaultois and A. P. Grosvenor, *J. Mater. Chem.*, 2011, **21**, 1829–1836.

39  A. P. Grosvenor and J. E. Greedan, *J. Phys. Chem. C*, 2009, **113**, 11366-11372.

40  E. R. Aluri, J. R. Hayes, J. D. S. Walker and A. P. Grosvenor, *J. Phys. Chem. C*, 2014, **15** 7910–7922.

41  E. R. Aluri and A. P. Grosvenor, *J. Alloys Comp.,* 2014, **616**, 516–526

42  PANalytical B. V. X'Pert HighScore Plus, Version 3.0, Almelo, The Netherlands, 2011.

43  S. M. Heald, D. L. Brewe, E. A. Stern, K. H. Kim, F. C. Brown, D. T. Jiang, E. D. Crozier and R. A. Gordon, *J. Synchrotron Rad.*, 1999, **6**, 347–349

44  A. Thompson, D. Attwood, E. Gullikson, M. Howells, K. J. Kim, J. Kirz, J. Kortright, I. Lindau, P. Pianetta and A. Robinson, *X-ray Data Booklet*, Lawrence Berkeley National Laboratory, Berkeley, CA, 2009.

45  X-ray Attenuation Length. http://henke.lbl.gov/optical_constants/atten2.html

46  Y. F. Hu, L. Zuin, R. Reininger and T. K. Sham, *AIP Conf. Proc.*, 2007, **879**, 535−538.

47  B. Ravel and M. Newville, *J. Synchrotron Rad.*, 2005, **12**, 537-541.

48  K. Kihara, *Eur. J. Mineral.*, 1990, **2**, 63-77.

49  J. Singh, D. Singh, S. P. Singh, G. S. Mudahar and K. S. Thind, *Mater. Phys. Mech*., 2014, **19**, 9-15.

50  S. Petrescu, M. Malki, M. Constantinescu, E. M. Anghel, I. Atkinson, R. State and M. Zaharescu*, J. optoelectron. Advan. Mater*., 2012, **14**, 603 – 612

51  Krinsley and H. David, Cambridge University Press, 1998.

52  T. Yamamoto, *X-Ray Spectrom*, 2008, **37**, 572-584.

53  L. A. Grunes, *Phys. Rev. B,* 1983, 27, 2111–2131.

54  D. Cabaret, A. Bordage, A. Juhin, M. Arfaoui and E. Gaudry, *Phys. Chem. Chem. Phys.,* 2010, **12**, 5619–5633.

55  D. Cabaret, Y. Joly, H. Renevier and C. R. Natoli, *J. Synchrotron Rad.*, 1999, **6**, 258-260.

56  M. W. Gaultois and A. P. Grosvenor, *Phys. Chem. Phys. Chem.*, 2011, **21**,1829-1836.

57  G. A. Waychunas, *Am. Mineral.*, 1987, **72**, 89-101.

58  F. Farges, G. E. Brown and J. J. Rehr, *Phys. Rev. B*, 1997, **56**, 1809-1819.

59  F. Farges, *Am. Mineral.*, 1997, **82**, 44-50.

60  G. Berlier, G. Spoto, S. Bordiga, G. Ricchiardi, P. Fisicaro, A. Zecchina, I. Rossetti, E. Selli, L. Forni and E. Giamello, *J. Catal.*, 2002, **208**, 64–82.

61  D. Li, G. M. Bancroft and M. E. Fleet, *Am. Mineral.*, 1996, **81**, 111–118.

62  D. Li, G. M. Bancroft, M. Kasrai, M. E Fleet, X. H. Feng, K.H. Tan and B. X. Yang, *Solid State Commun.*,1993, **87**, 613–617.

63  D. Li, G. M. Bancroft, M. Kasrai, M. E. Fleet, X. H. Feng and K. H. Tan, *Am. Mineral.*, **79**, 785–788.

64  L. A. J. Garvie and P. R. Buseck, *Am. Mineral.*, 1999, **84**, 946–964.

65  G. R. Harp, D. K. Saldin and B. P. Tonner, *I. Phys.: Condens. Matter.*, 1993, **5**, 5377-5388.

66  D. Li, G. M. Bancroft, M. Kasrai, M. E. Fleet, R. A. Secco, X. H. Feng, K. H. Tan and B. X. Yang, *Am. Mineral.*, 1994, **79**, 622-632.

67  J. R. Hayes and A. P. Grosvenor, *J. Alloys Comp.*, 2012, **537**, 323–331.

68 J. A. Sigrist, M. W. Gaultois and A. P. Grosvenor, *J. Phys. Chem. A*, 2011, **115**, 1908-1912.

69 T. E. Westre, P. Kennepohl, J. G. DeWitt, B. Hedman, K. O. Hodgson and E. I. Solomon, *J. Am. Chem. Soc.*, 1997, **119**, 6297-6314.

70 B. Mehdikhani and G. H. Borhani, *Process. Appl. Ceram.*, 2013, **7**, 117–121.

71 V. Magnien, D. R. Neuville , L. Cormier, J. Roux, J. L. Hazemann, D. de Ligny, S. Pascarelli, I. Vickridge, O. Pinet and P. Richet, *Geo. Cosmo. Acta*, 2008, **72**, 2157-2168.

72 V. Magnien, D. R. Neuville, L. Cormier, J. Roux, J. L. Hazemann, O. Pinet and P. Richet, *J. Nucl. Mater.,* 2006, **352**, 190–195.

73 R. K. Kukkadapu, H. Li, G. L. Smith, J. D. Crum, J. Jeoung, W. H. Poisl and M. C. Weinberg, *J. Non-Cryst. Sol.*, 2003, **317**,301–318.

74 J. D. S. Walker and A. P. Grosvenor, I*norg. Chem.*, 2013, **52**, 8612–8620.

**Tables**
**Table 1: Compositions of the different glasses synthesized.**

| Glass | SiO$_2$ (mol %) | B$_2$O$_3$ (mol %) | Na$_2$O (mol %) | CaO (mol %) | Fe$_2$O$_3$ (mol %) | Al$_2$O$_3$ (mol %) |
|---|---|---|---|---|---|---|
| Borosilicate (BG) | 63.5 | 16.9 | 16.5 | 3.1 | - | - |
| Fe-Al-borosilicate (FABG) | 55.5 | 16.9 | 16.5 | 3.1 | 3.0 | 5.0 |
| Fe-borosilicate (FBG) | 60.5 | 16.9 | 16.5 | 3.1 | 3.0 | - |
| Al-borosilicate (ABG) | 58.5 | 16.9 | 16.5 | 3.1 | - | 5.0 |

**Table 2 Labels used to name the glasses and glass-ceramic composites studied.**

| Label | Sample description |
|---|---|
| BG | Borosilicate glass |
| FABG | Fe-Al-borosilicate glass |
| FBG | Fe-borosilicate glass |
| ABG | Al-borosilicate glass |
| BG-Gd$_2$Ti$_2$O$_7$-1100 $^o$C/750 $^o$C | Borosilicate glass- Gd$_2$Ti$_2$O$_7$ composite materials annealed at 1100 $^o$C or 750 $^o$C |
| FABG-Gd$_2$Ti$_2$O$_7$-1100 $^o$C/750 $^o$C | Fe-Al-borosilicate glass- Gd$_2$Ti$_2$O$_7$ composite materials annealed at 1100 $^o$C or 750 $^o$C |

**Table 3 Calculated glancing angles required to give specific X-ray attenuation depths in Gd$_2$Ti$_2$O$_7$ for photons having energies of 4966 eV (Ti K-edge).**

| Ti K-edge (4966 eV) | |
| --- | --- |
| X-ray attenuation depth (nm) | Glancing angle |
| 220 | 1.4$^o$ |
| 450 | 4.5$^o$ |
| 4088 | 45$^o$ |

**Figure Captions**

**Figure 1:** A portion of the pyrochlore-type structure adopted by $Gd_2Ti_2O_7$ is shown. The structure consists of $GdO_8$ in a distorted cubic polyhedra (dark grey) and distorted $TiO_6$ octahedra (light grey). The O atoms (dark grey spheres) occupy tetrahedral interstitial sites. The structure was generated using the VESTA program.[33]

**Figure 2:** XRD patterns from the (a) Borosilicate glass (BG) and the BG-ceramic composite materials annealed at $1100^oC$ and (b) Fe-Al-borosilicate glass (FABG) and the FABG-ceramic composite materials (20 wt%, 40 wt%, and 80 wt% loading of $Gd_2Ti_2O_7$) annealed at $1100^oC$ are shown. The patterns from the glass materials are also shown.

**Figure 3:** XRD patterns from the (a) Borosilicate and its composite materials annealed at $750^oC$ and (b) Fe-Al-borosilicate glass and its composite materials (10 wt%, 20 wt%, 40 wt%, and 80 wt% loading of $Gd_2Ti_2O_7$) annealed at $750^oC$ are shown. Diffraction peaks from quartz are marked by an asterisk (*). Patterns from (c) Fe-borosilicate glass (FBG) and (d) Al-borosilicate glass (ABG) annealed at $750^oC$ are also shown.

**Figure 4:** (a,b,c) Backscattered images from the borosilicate glass composite materials (20 wt% , 40 wt%, and 60 wt% loading of $Gd_2Ti_2O_7$, respectively) annealed at $750^oC$. (d) Backscattered electron image from the borosilicate glass composite materials (20 wt% and 40 wt% $Gd_2Ti_2O_7$, respectively) annealed at $1100^oC$. The scale bar in each image is 10 μm.

**Figure 5:** Ti K-edge XANES spectra from BG-$Gd_2Ti_2O_7$-$1100^oC$ and FABG-$Gd_2Ti_2O_7$-$1100^oC$ containing 20 wt% , 50 wt%, and 80 wt% loading of $Gd_2Ti_2O_7$ are shown. The spectra are compared to the spectrum from $Gd_2Ti_2O_7$. Feature A represents the pre-edge region (1s→3d) and is shown in the inset. Feature B and C (1s→4p) represent the main-edge region. The arrows

show the changes in intensity and energy of spectral features that occur with increasing loading of $Gd_2Ti_2O_7$.

**Figure 6:** Ti K-edge XANES spectra from BG-$Gd_2Ti_2O_7$-750$^{\circ}$C and FABG-$Gd_2Ti_2O_7$-750$^{\circ}$C containing 20 wt% , 50 wt%, and 80 wt% loading of $Gd_2Ti_2O_7$. The spectra are compared to the spectrum from $Gd_2Ti_2O_7$. Arrows mark the changes observed in the spectra with increasing loading of $Gd_2Ti_2O_7$.

**Figure 7:** (a) Ti K-edge XANES spectra from BG- and FABG- composite materials (50 wt% $Gd_2Ti_2O_7$) annealed at 1100$^{\circ}$C are shown. (b) Ti K-edge XANES spectra from BG-$Gd_2Ti_2O_7$-750$^{\circ}$C, FABG-$Gd_2Ti_2O_7$-1100$^{\circ}$C and FABG-$Gd_2Ti_2O_7$-750$^{\circ}$C containing the same loading of $Gd_2Ti_2O_7$ are shown.

**Figure 8:** Si $L_{2,3}$-edge XANES spectra from the borosilicate glass annealed at 1100$^{\circ}$C or 750$^{\circ}$C are shown. The spectra are compared to the spectrum of amorphous $SiO_2$ that was reported previously.

**Figure 9:** Si $L_{2,3}$-edge XANES spectra from (a) BG-$Gd_2Ti_2O_7$-1100$^{\circ}$C and (b) FABG-$Gd_2Ti_2O_7$-1100$^{\circ}$C containing 20 wt% , 50 wt%, and 80 wt% loading of $Gd_2Ti_2O_7$ are shown. The spectra are compared to the spectrum from the corresponding glass. Features C and D become narrower to higher energy with increasing loading of $Gd_2Ti_2O_7$.

**Figure 10:** Si $L_{2,3}$-edge XANES spectra from (a) BG-$Gd_2Ti_2O_7$-750$^{\circ}$C and (b) FABG-$Gd_2Ti_2O_7$-750$^{\circ}$C containing 80 wt% , 50 wt%, and 20 wt% loading of $Gd_2Ti_2O_7$ are shown. The spectra are compared to the spectrum from the corresponding glass.

**Figure 11:** (a). The Fe K-edge XANES spectrum from FABG is compared to the spectra from FeO ($Fe^{2+}$) and $Fe_2O_3$ ($Fe^{3+}$). (b,c) Fe K-edge XANES spectra from FABG-$Gd_2Ti_2O_7$-1100°C and FABG-$Gd_2Ti_2O_7$-750°C containing 20 wt% , 50 wt%, and 80 wt% loading of $Gd_2Ti_2O_7$ are shown. These spectra are compared to the spectrum from FABG. Shifts in the absorption energy of the composite materials annealed at different temperatures as compared to the spectrum from FABG are indicated using arrows.

**Figure 12:** Ti K-edge GA-XANES spectra from (a) BG-$Gd_2Ti_2O_7$-1100 °C (60 wt% loading of $Gd_2Ti_2O_7$) and (b,c,d) BG-$Gd_2Ti_2O_7$-750 °C (20 wt%, 40 wt%, and 60 wt% loadings of $Gd_2Ti_2O_7$) implanted using $Au^-$ ions to a dose of $5\times10^{14}$ ions/$cm^2$ are shown. These spectra are compared to the spectrum from the as-synthesized composite materials. The angles listed, 1.4°, 4.5° and 45°, are the glancing angles used to attain X-ray penetration depths of 220, 450, and 4088 nm, respectively. The changes observed in the spectra with decreasing glancing angle are indicated by arrows.

**Figure 13:** (a) Ti K-edge GA-XANES spectra from BG-$Gd_2Ti_2O_7$-750°C (40 wt% loading of $Gd_2Ti_2O_7$) and $Gd_2Ti_2O_7$ implanted to a dose of $5\times10^{14}$ ions/$cm^2$ are shown. The glancing angle was adjusted for each sample to give an X-ray attenuation depth of 220 nm.
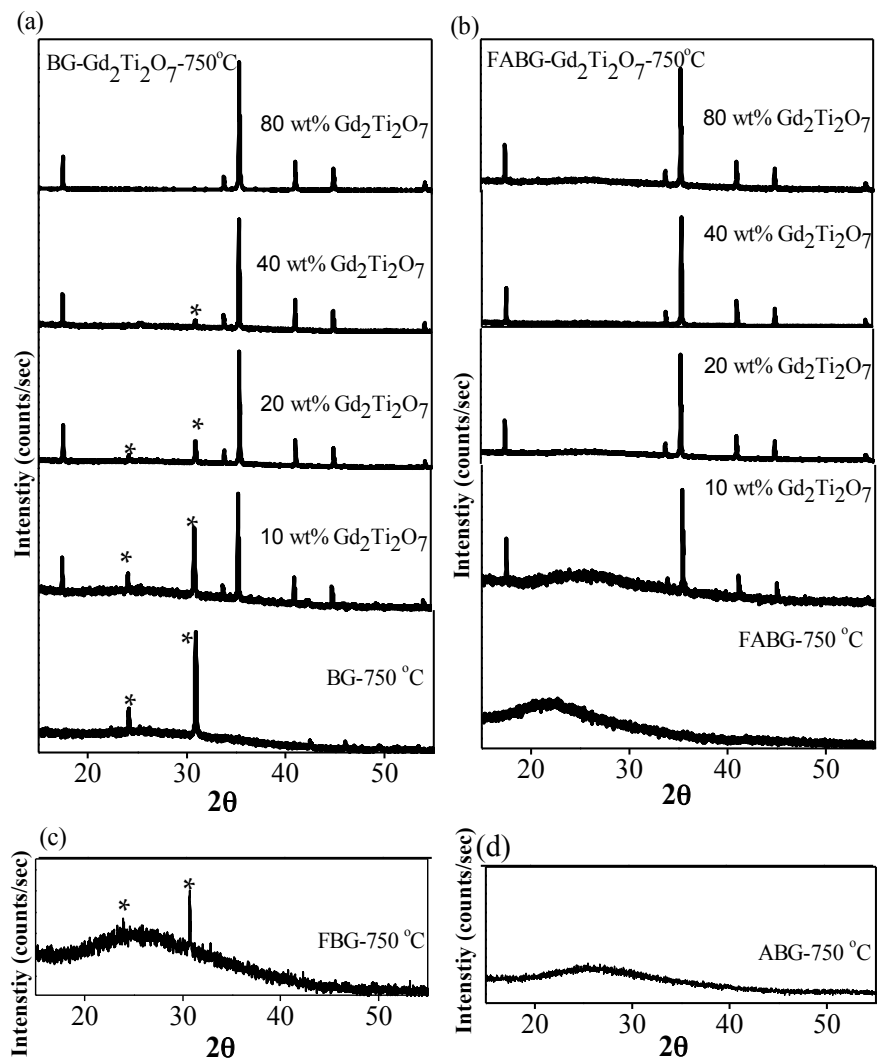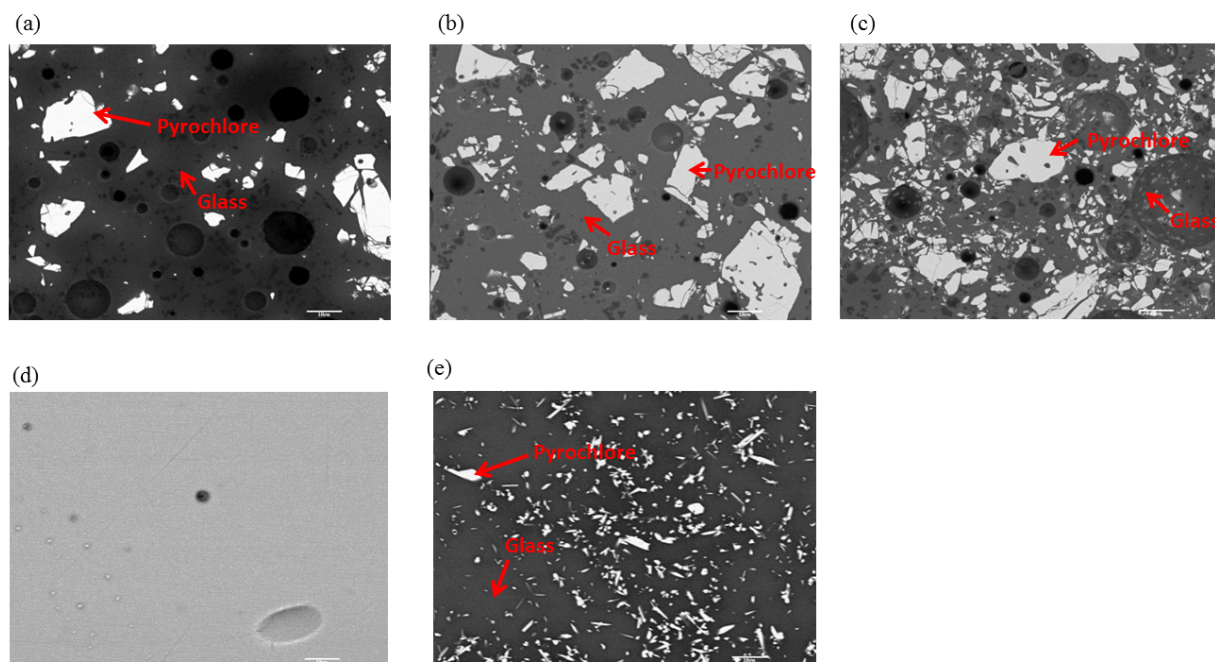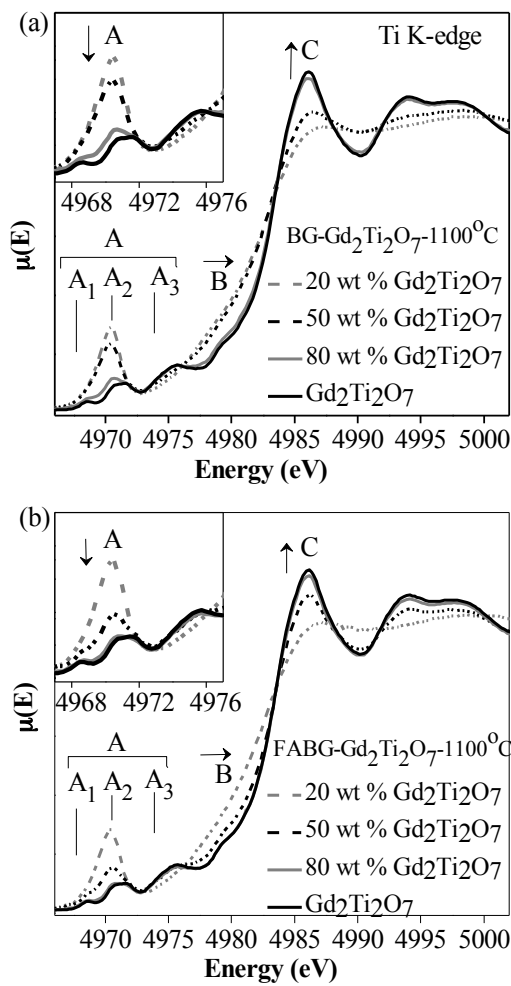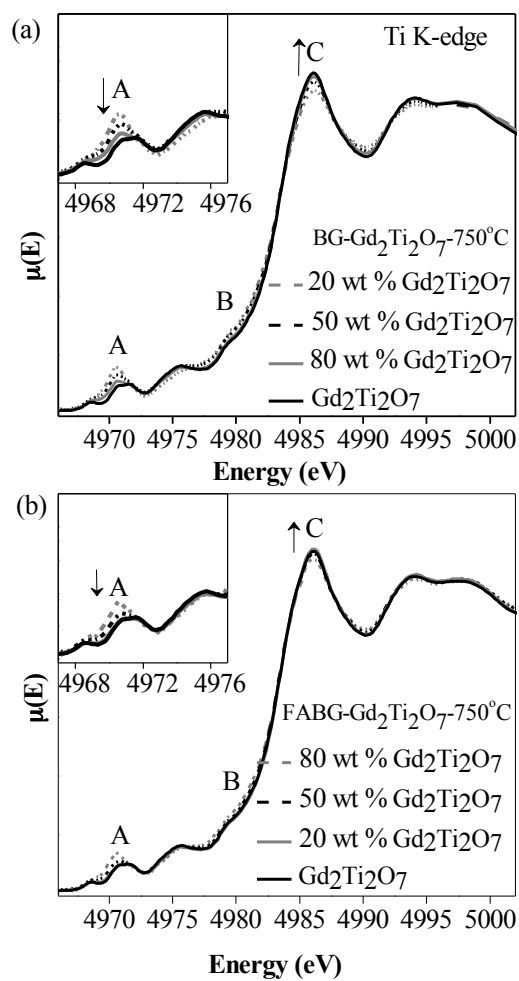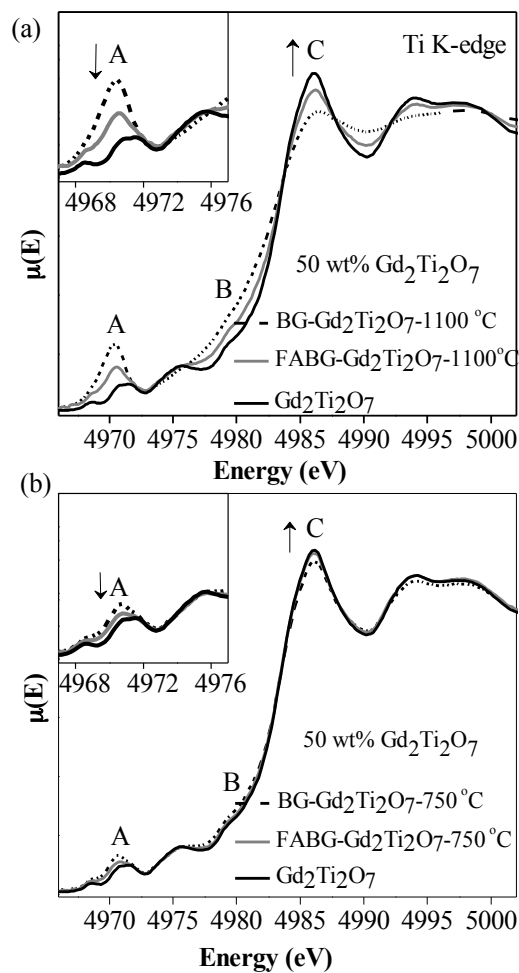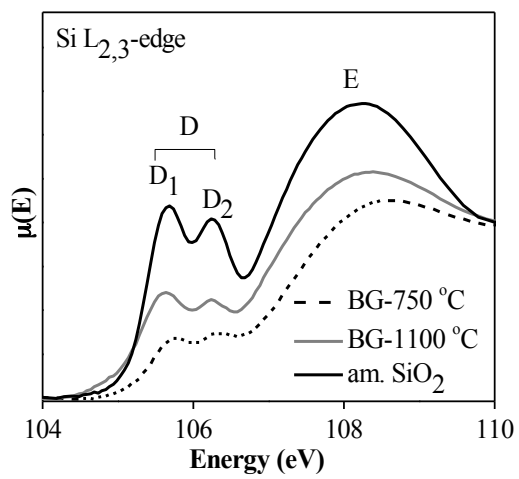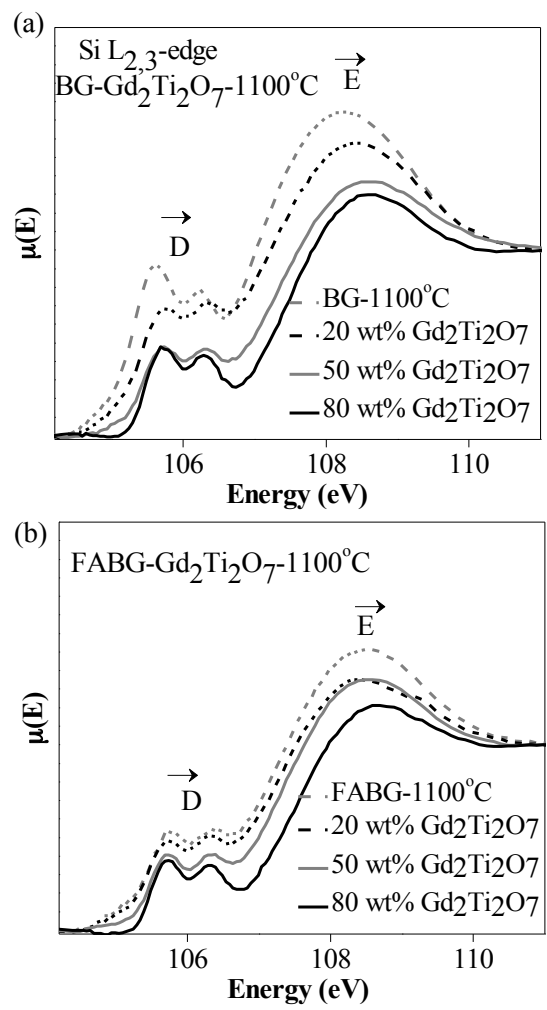
Figure 1
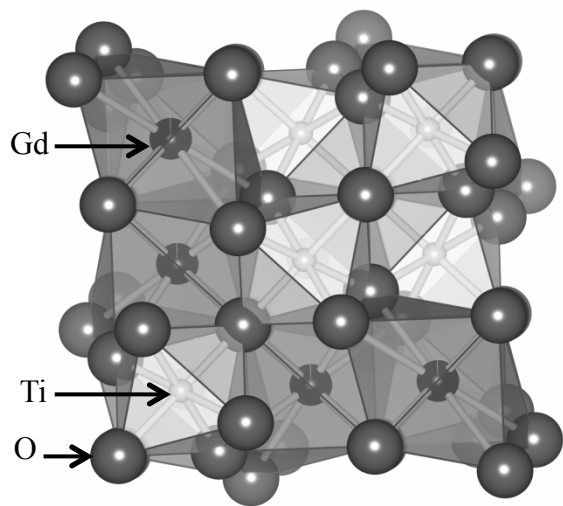
Figure 2
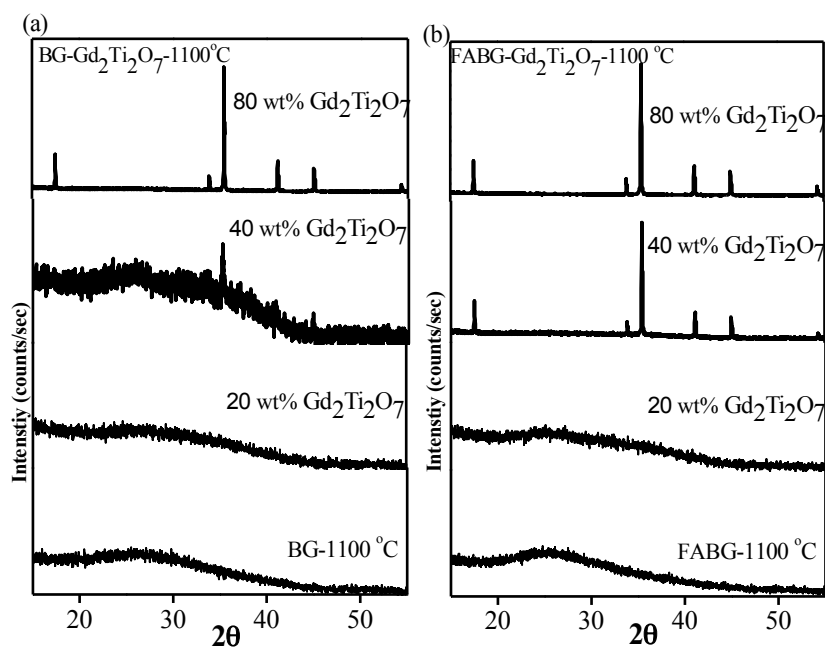
Figure 3

Figure 4

Figure 5

Figure 6

Figure 7

Figure 8

Figure 9

Figure 10
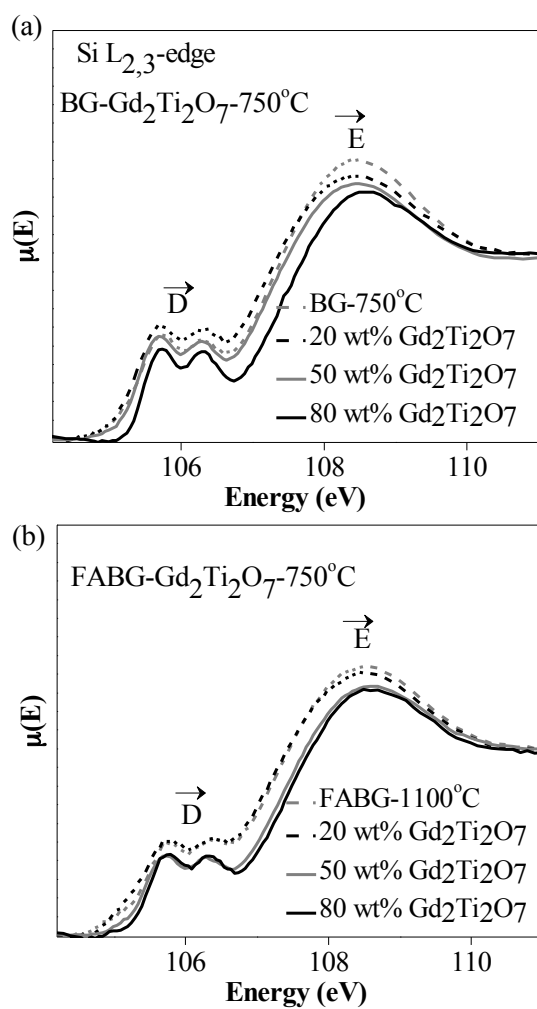
Figure 11

Figure 12

Figure 13



Ti K-edge
GA-XANES

$5 \times 10^{14}$ ions/cm$^2$
220 nm-1.4$^{\circ}$
40 wt % Gd$_2$Ti$_2$O$_7$

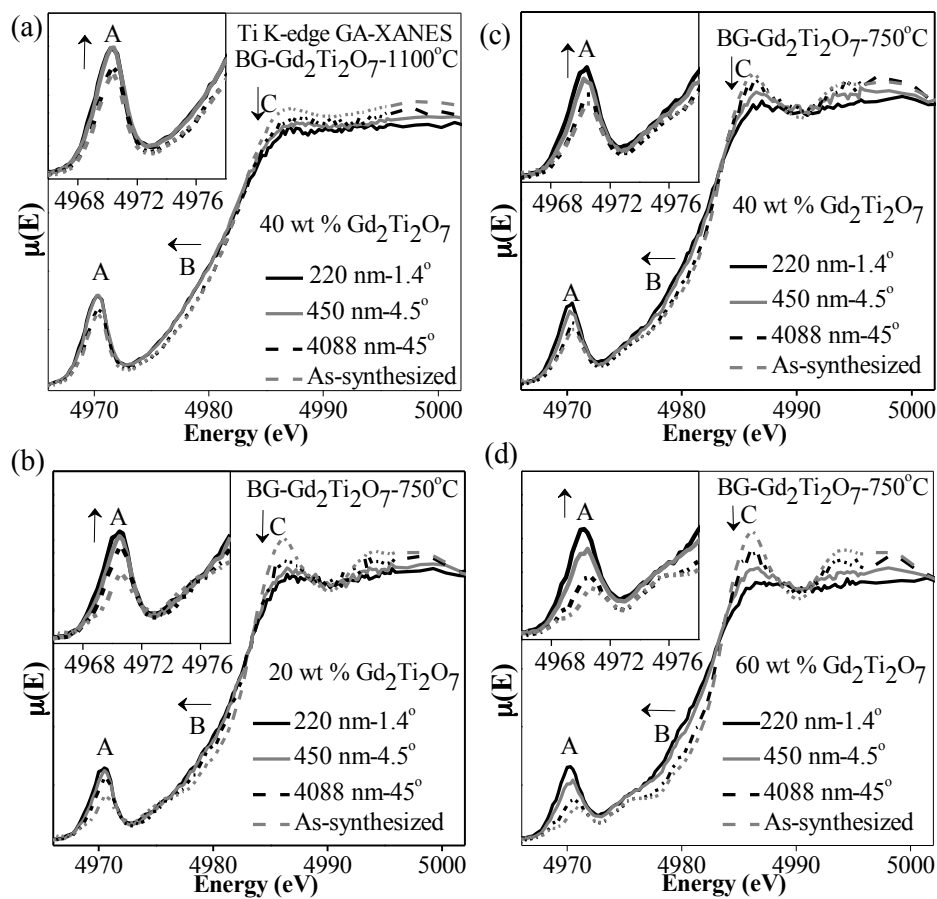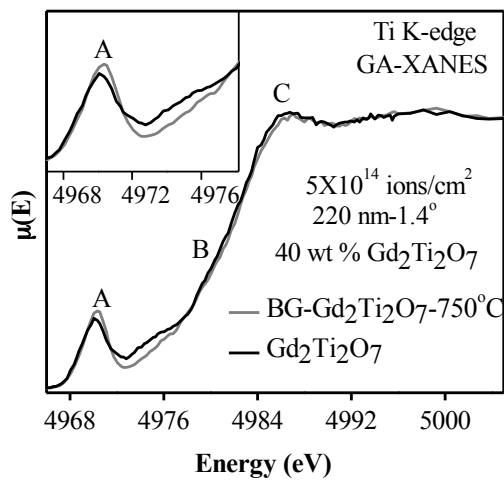— BG-Gd$_2$Ti$_2$O$_7$-750$^{\circ}$C
— Gd$_2$Ti$_2$O$_7$

μ(E)

Energy (eV)
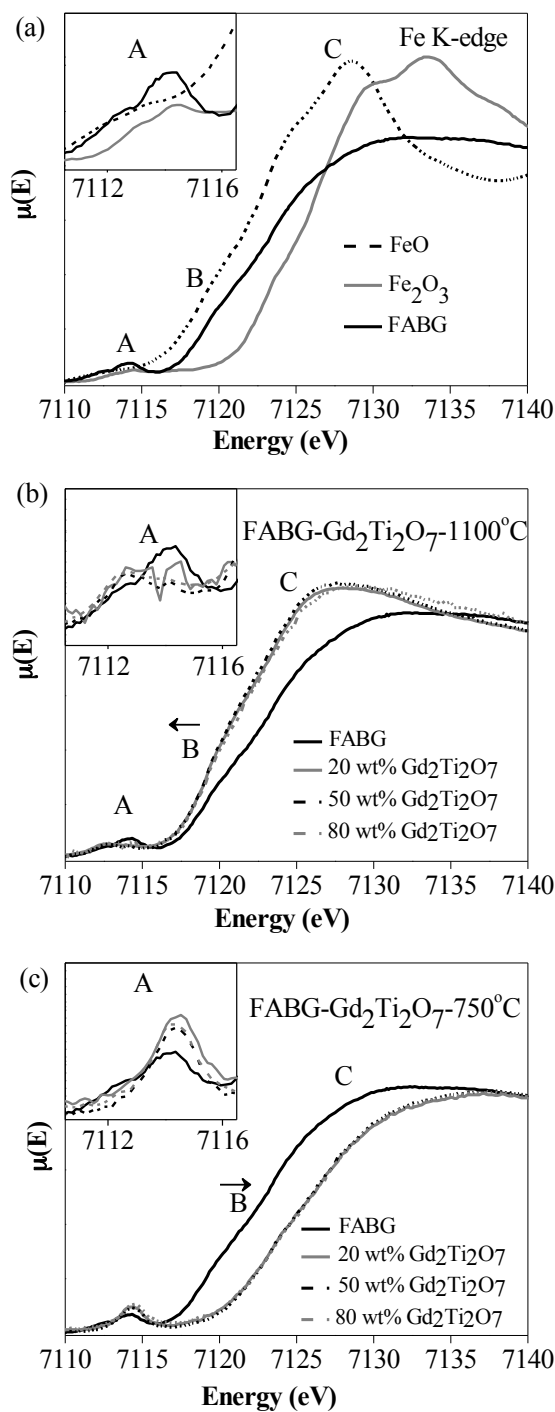
43

Table of contents image (TOC):